Advances and Applications in Fluid Mechanics

https://pphmjopenaccess.com
https://doi.org/10.17654/0973468625006
Volume 32, Number 2, December 2025, Pages 93-136 **P-ISSN: 0973-4686**

BASE PRESSURE CONTROL AND TEMPERATURE DISTRIBUTION ALONG THE DUCT AT SUPERSONIC MACH NUMBER: A COMPREHENSIVE CFD APPROACH-PART I

Amirullah Jais[1], Ambareen Khan[2], Mohammad Nishat Akhtar[3] and Sher Afghan Khan[4,*]

[1]Department of Mechanical and Aerospace Engineering
International Islamic University Malaysia
Kuala Lumpur, 53100
Malaysia
e-mail: amirerrol@gmail.com

[2]Centre for Instructional Technology and Multimedia
Universiti Sains Malaysia
11800 USM, Pulau Pinang
Malaysia
e-mail: khanambareen5@gmail.com

Received: June 11, 2025; Accepted: July 30, 2025
2020 Mathematics Subject Classification: 76D10.
Keywords and phrases: base flow, L/D ratio, Mach number, CFD.
*Corresponding author

How to cite this article: Amirullah Jais, Ambareen Khan, Mohammad Nishat Akhtar and Sher Afghan Khan, Base pressure control and temperature distribution along the duct at supersonic Mach number: a comprehensive CFD approach-Part I, Advances and Applications in Fluid Mechanics 32(2) (2025), 93-136. https://doi.org/10.17654/0973468625006

Published Online: August 20, 2025

[3]School of Aerospace Engineering
Universiti Sains Malaysia
14300 Nibong Tebal, Penang, Malaysia
e-mail: nishat@usm.my

[4]Department of Mechanical and Aerospace Engineering
Faculty of Engineering
International Islamic University
Kuala Lumpur, 53100, Malaysia
e-mail: sakhan@iium.edu.my

Abstract

Sudden expansion is widespread in industry and at the base of rockets and missiles. Managing base pressure in supersonic flows is crucial for reducing drag and enhancing the performance of high-speed vehicles, such as missiles and rockets. This study investigates the use of quarter-circular ribs to regulate base pressure as a passive control method. Computational simulations investigate how the rib radius and placement near a backward-facing step influence flow behavior, including recirculation and vortex formation. In the study, the inertia parameters considered were a Mach number of $M = 1.7$ and the nozzle pressure ratio (NPR) in the range of 3 to 11. The geometrical parameters considered were the area ratio $(A_2/A_1 = 4)$, the cross-sectional area of the duct-to-nozzle exit, and the length-to-diameter (L/D) ratio, ranging from 1 to 6. The quarter-circle radii considered were 1.5 mm, 2 mm, and 3 mm, and the ribs were located at $L/D = 0.5$, 1, 1.5, and 2. The goal is to identify the optimal rib geometry and location that maximizes aerodynamic efficiency. The results show that the optimum rib radius and locations are 3 mm and $L/D = 2$. The rib radius of 1.5 mm does not show any definite pattern. In contrast, the 3 mm rib radius exhibits a progressive increase in the base at various locations within the duct. This study includes the results for the rib facing the curved part of the rib only. Hence, a 3 mm rib radius seems to be the best option if the application is to reduce the base drag to a considerable level.

1. Introduction

The study of turbulent base flows has gained significant attention due to its wide-ranging applications in aerospace, defense, and industrial systems. These flows, commonly observed around blunt-based projectiles and fuselages, often exhibit sub-atmospheric pressure and complex aerodynamic interactions. As the flow separates and reattaches, it forms distinct recirculation zones and shear layers, generating strong vortices that contribute to drag. The flow becomes highly chaotic at sonic speeds, further complicating pressure distribution [1].

The sudden expansion of a gas jet is a common issue in various flow systems. Usually, the enlarged duct has a smooth, continuous inner surface. It relies on the low base pressure created by the rapid relaxation of the shear layer at the inlet, which is then suddenly expanded. The vortex dynamics caused by this flow expansion control the base pressure and the flow field downstream. However, this work focuses on air jets that expand suddenly into a larger duct with annular cavities before releasing into the atmosphere. In this case, the base pressure and flow development downstream are influenced by both the primary vortices generated by the shear layer expansion at the base and the secondary vortices created by the cavities in the enlarged duct. Some related studies are discussed.

Drag in high-speed aerodynamics comprises multiple components: base drag, wave drag, and skin friction drag. While skin friction and base drag dominate at subsonic speeds, wave drag becomes critical in supersonic regimes. Base pressure plays a pivotal role in aerodynamic efficiency, particularly for rockets and missiles, where optimizing it can significantly reduce drag. However, factors like skin friction and shock-induced wave drag are inherent to high-speed flight and cannot be easily mitigated without compromising performance [2, 3].

Active and passive controls are the two methods used to control the base pressure. Blowing or suction techniques are used to achieve dynamic control of base fluxes, which necessitate an outside energy source. Its ability to be

turned on and off as needed is the primary benefit of this kind of control. The primary drawback of this type of control is the reliance on a high-energy source and the additional weight it imposes on aeronautical vehicles, such as rockets and launch vehicles, where weight is a crucial factor. Obtaining a second external energy source is not always possible.

While active methods, such as jet injection, improve pressure recovery, passive approaches remain more practical for real-world implementation. Research indicates that base drag can account for 60-70% of total drag at transonic speeds, yet the underlying mechanisms remain poorly understood. Passive techniques, such as strategically placed ribs, present a promising solution for drag reduction without additional energy input.

This study employs a regulation of base pressure through passive control using quarter-circular ribs for an area ratio of 4 at a supersonic Mach number of Mach 1.7. By altering the flow field near the base, quarter ribs can effectively manipulate base pressure. Optimizing the geometry of these passive control devices is crucial, as any increase in base pressure and consequent decrease in base drag will significantly affect the aerodynamic efficiency.

2. Literature Review

Suddenly, expanded flows at sonic and supersonic Mach numbers present complex challenges due to flow separation, recirculation zones, and base pressure deficits, which contribute significantly to aerodynamic drag. Researchers have extensively explored passive control methods, such as incorporating ribs, cavities, and other geometric modifications, to mitigate these issues and enhance base pressure recovery. Khan et al. [1] conducted experimental investigations on the use of semi-circular ribs in suddenly expanded flows at both sonic and supersonic Mach numbers. Their study compared experimental results with predictions from single-layer and deep neural network models, demonstrating that the inclusion of ribs effectively increased base pressure and reduced flow separation.

In a complementary study, Khan et al. [2] examined the effect of ribs as passive control devices on base pressure at sonic Mach numbers. Their findings indicated that the presence of ribs led to a significant increase in base pressure, attributed to the disruption of the recirculation zone and the promotion of earlier flow reattachment. Further exploring rib geometries, Khan et al. [3] analyzed the impact of various rib configurations in a suddenly expanded flow at sonic Mach numbers. The study revealed that specific rib shapes and placements could optimize base pressure recovery, highlighting the importance of geometric considerations in passive control strategies. Numerical simulations have also played a pivotal role in understanding flow behaviors. Khan et al. [4] performed simulations of suddenly expanded flows from converging nozzles at sonic Mach numbers, providing insights into velocity distributions and base pressure variations. Their work highlighted the importance of nozzle geometry and expansion ratios in shaping flow characteristics.

Advancements in computational fluid dynamics (CFD) have facilitated more comprehensive analyses. Khan et al. [5] conducted a CFD study on base pressure control using quarter ribs in sudden expansion ducts at sonic Mach numbers. The research demonstrated that quarter ribs could effectively manipulate the flow field, leading to enhanced base pressure and reduced drag. Building upon this, Khan et al. [6] explored the use of semi-circular ribs at critical Mach numbers. Their findings emphasized the effectiveness of these ribs in controlling base pressure, particularly at specific Mach number regimes.

Nurhanis et al. [7] investigated base pressure control at supersonic Mach numbers in suddenly expanded flows, emphasizing the role of passive devices in managing shock-boundary layer interactions. Their findings indicated that appropriately designed control elements could mitigate adverse pressure gradients and stabilize the flow. Ahmad Fakhruddin et al. [8] analyzed base pressure control with ribs at Mach 1.2 using CFD methods. The study highlighted the effectiveness of rib placements in altering flow

structures and improving pressure distributions, reinforcing the utility of passive controls in supersonic applications.

Khan et al. [9] examined velocity distribution and base pressure analysis of under-expanded nozzle flow at Mach 1.0. Their research provided valuable data on flow characteristics in such conditions, aiding in the design of effective control strategies. Incorporating machine learning, Khan et al. [10] assessed the performance of supervised learning algorithms in classifying flow behaviors. Their work suggested that machine learning techniques can complement traditional computational fluid dynamics (CFD) methods in designing efficient flow control mechanisms. Mishra et al. [11] focused on determining shock standoff distances for wedges in supersonic flow, contributing to the understanding of shock-wave interactions in high-speed flows.

Chaudhary et al. [12] explored base pressure control using quarter-circle ribs in suddenly expanded ducts at screech-prone Mach numbers $(M = 1.8)$. Their study demonstrated the potential of such ribs in mitigating screech phenomena and enhancing flow stability. Mahaboobali et al. [13] investigated the passive control of base flows, analyzing the impact of quarter-rib radius and locations at sonic Mach numbers. Their findings emphasized the importance of rib geometry and placement, as they are not effective for flow control. Further, Chaudhary et al. [14] studied the control of suddenly expanded flow using quarter ribs for an area ratio of 4.84 at Mach 2. Their research highlighted the significance of area ratios in designing effective passive control mechanisms. Khan et al. [15] conducted an extensive CFD study on supersonic flow control with quarter ribs in ducts. Their work provided comprehensive insights into the effectiveness of quarter ribs across various flow conditions. Shetty et al. [16] performed a comprehensive CFD analysis on base pressure control using quarter ribs at Mach 1.3. Their study reinforced the utility of quarter ribs in managing base pressure across different Mach numbers. Bellary et al. [17] conducted numerical simulations of base pressure and its control in suddenly expanded

ducts at Mach 1.6 using quarter-circular ribs. Their findings contributed to the optimization of rib designs for effective flow control.

In another study, Bellary et al. [18] analyzed the computational aspects of thrust generated by converging-diverging nozzles at different diverging angles. Their research provided valuable data for optimizing nozzle designs in high-speed applications. Anuar et al. [19] investigated the effect of cavity geometry and location on base pressure in suddenly expanded flows at Mach 2.0 for an area ratio of 3.24. Their study emphasized the role of cavity design in passive flow control strategies. Bashir et al. [20] conducted a numerical investigation of turbulence models with an emphasis on turbulent intensity at low Reynolds number flows. Their work contributed to the selection of appropriate turbulence models for accurate flow simulations.

Baig et al. [21] explored the control of base flows with micro-jets, demonstrating the effectiveness of active control methods in managing base pressure and reducing drag. Rehman and Khan [22] focused on controlling base pressure with micro-jets, providing insights into the design and implementation of active flow control techniques.

Faheem et al. [23] conducted an experimental study on the mean flow characteristics of a supersonic multiple jet configuration, contributing to the understanding of complex jet interactions in high-speed flows. Sajali et al. [24] performed a numerical investigation of the flow field of a non-circular cylinder, providing data relevant to flow control around bluff bodies. Khan et al. [25] investigated the passive flow control management of base drag in compressible subsonic flow using multiple cavities, emphasizing the effectiveness of cavity configurations in reducing drag.

In another study, Khan et al. [26] conducted a computational fluid dynamics (CFD) analysis of a human-powered submarine to minimize drag, applying flow control principles to underwater vehicles. Khan et al. [27] investigated the passive control of base drag employing dimples in subsonic suddenly expanded flow, demonstrating the potential of surface

modifications in drag reduction. Aabid et al. [28] optimized the dry sliding wear behavior of aluminum-based hybrid metal matrix composites using experimental and design of experiments (DOE) methods, contributing to material selection in flow control applications.

Based on the above literature review, the authors believe that no study has been conducted for a screech-prone Mach number $M = 1.7$ and an area ratio of 4. The findings of this study will be convenient in the design and development of aerospace vehicles. The database obtained through this study can be used to find the optimum dimensions of the rockets and missiles. Any increase in the base pressure, and hence a decrease in the total base drag, will be beneficial in arriving at the optimum design of aerospace launch vehicles.

3. Methodology: Finite Volume Method

3.1. Governing equations

The following hypotheses are taken into consideration:

(i) Turbulent flow is considered because of the turbulent viscous dissipation effects.

(ii) The fluid's viscosity varies with temperature and is compressible.

(iii) At atmospheric pressure, the flow exits the duct.

(iv) Khan et al. [16] employed the standard k-ε turbulence model to simulate the internal flow. As a result, the standard k-ε turbulence model is applied to the circumstance. Sutherland's three-coefficient viscosity model is expressed as follows:

$$\mu' = \mu'_o \left(\frac{T_a}{T_{a,o}} \right)^{3/2} \frac{T_{a,o} + S'}{T_a + S'}. \tag{1}$$

The reference viscosity value in kg/m-s is denoted as μ'_o, where μ' represents the viscosity. T_a denotes static temperature, and S' is the temperature-dependent Sutherland constant.

Continuity equation for unsteady compressible flow

The equation for mass balance is as follows:

$$\frac{\partial \rho}{\partial t} + \underline{\nabla} \cdot (\rho \underline{V}) = 0, \tag{2}$$

where the fluid's velocity is denoted by V.

The equation for momentum balance is:

$$\frac{\partial}{\partial t}(\rho \underline{V}) + \underline{\nabla} \cdot (\rho \underline{\underline{V}}\underline{V}) + \underline{\nabla} p = \underline{\nabla} \cdot [2\mu (\underline{\underline{\nabla V}})_o^s] + \underline{\nabla} \cdot (\tau_{=Re}), \tag{3}$$

where $(\underline{\underline{\nabla V}})_o^s = (\underline{\underline{\nabla V}})^s - \frac{1}{3}(\underline{\nabla} \cdot \underline{V})\underline{I}$, $(\underline{\underline{\nabla V}})^s = \frac{\underline{\underline{\nabla V}} + \underline{\underline{\nabla V}}^T}{2}$, and $\tau_{=Re}$ is the turbulent stress tensor.

The formulae for total energy are as follows:

$$\frac{\partial}{\partial t}\left[\rho\left(\frac{1}{2}V^2 + u_{\text{int}}\right)\right] + \underline{\nabla}\left[\rho\left(\frac{1}{2}V^2 + u_{\text{int}}\right)\underline{V}\right]$$

$$= \underline{\nabla}(\lambda \underline{\nabla} T - p\underline{V} + 2\mu \underline{V} \cdot (\underline{\underline{\nabla V}})_o^s + \underline{V} \cdot \tau_{=Re}), \tag{4}$$

where u_{int} is the internal energy, and λ is the thermal conductivity.

Many internal flow simulations use the k-ε turbulence model due to its affordability, resilience, and sufficient accuracy. The Ansys Fluent program incorporates the k-ε turbulence model used in this research. The K-equation allowed us to calculate the turbulent kinetic energy:

$$\frac{\partial}{\partial t}(\rho k) + \underline{\nabla} \cdot (\rho \underline{V} k) = \underline{\nabla} \cdot \left[\left(\mu + \frac{\mu_t}{\sigma_k}\right)(\underline{\nabla} k)\right] - \rho\varepsilon + M_x. \tag{5}$$

The turbulent kinetic energy dissipation rate is denoted by ε, the turbulent Prandtl number is σ-k, and M_x is the turbulence generation. Precisely, the dissipation is controlled by

$$\frac{\partial(\rho\varepsilon)}{\partial t} = -\underline{\nabla}\cdot(\rho\varepsilon\vec{V}) + \underline{\nabla}\cdot\left[\left(\mu + \frac{\mu_T}{\sigma_\varepsilon}\right)\nabla\varepsilon\right] - C_1 f_1\left(\frac{\varepsilon}{k}\right)M - C_2 f_2 \frac{\varepsilon^2}{k}, \quad (6)$$

where $\mu_t = \rho f_\mu C_\mu k^2/\varepsilon$ denotes turbulent viscosity, and the arbitrary constants are denoted as $\overline{C_\mu} = 0.09$, $\overline{C_1} = 1.44$, $\overline{C_2} = 1.92$, $\overline{f_\mu} = 1$, $\sigma_k = 1.0$, and $\sigma_\varepsilon = 1.3$.

3.2. Geometry and modelling

The simulation procedure employed a finite volume method (FVM), specifically using Workbench 2024/R2 software to analyze the fluid flow in the nozzle. The model was designed as shown in Figure 1, with geometries listed in Table 1, and generated using a Design Modeler for two orientations, as depicted in Figure 2, with specified boundary conditions.

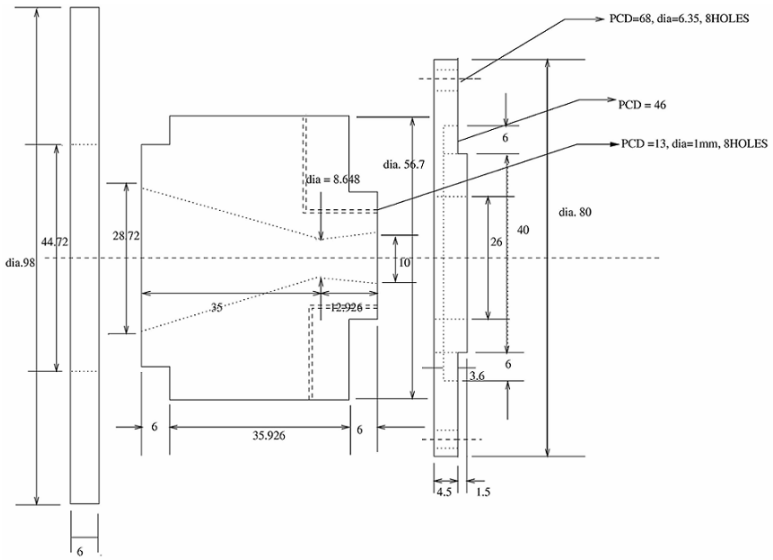

(a)

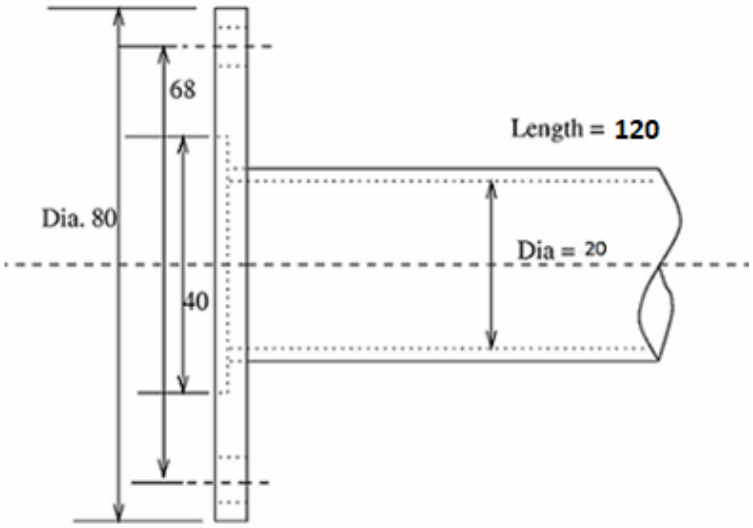

(b)

Figure 1. Nozzle and duct dimensions.

Table 1. Geometries of design model

Parameters	Dimensions
Nozzle inlet diameter	28.72 mm
Nozzle outlet diameter	10 mm
Nozzle throat diameter	8.468 mm
Converging nozzle length	35 mm
Diverging nozzle length	12.926 mm
Duct diameter	20 mm
Duct length	Varies from 1D to 6D
Rib radius	1 mm, 1.5 mm, 2 mm, 2.5 mm, 3mm
Rib locations	0.5D, 1D, 1.5D, 2D, 3D

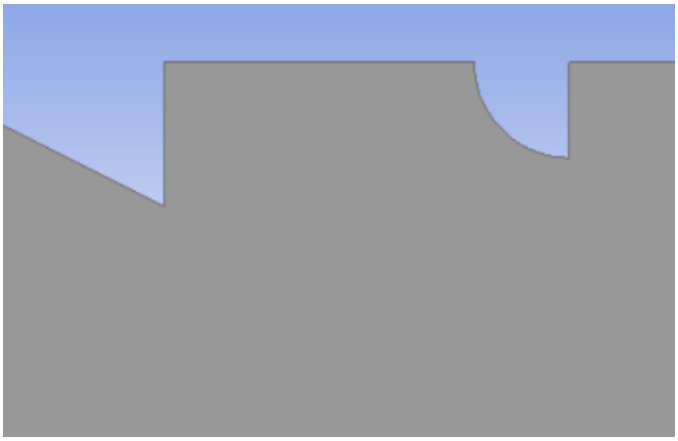

Figure 2. Rib orientations.

3.3. Meshing and boundary conditions

A high-quality mesh, characterized by good aspect ratios, smooth transitions between cells, and the absence of skewed or distorted elements, is crucial for accurate and efficient simulations. By choosing the free-face mesh type, the 2D model is of the structured mesh type in this case. CFD meshing involves dividing the computational domain into discrete cells or elements. A high-quality mesh, characterized by good aspect ratios, smooth transitions between cells, and the absence of skewed or distorted elements, is crucial for accurate and efficient simulations. Appropriate and refined face meshing, as shown in Figure 3, was employed, where a grid size was carefully determined to ensure convergence and reliable results. The mesh density should be sufficient to capture relevant flow features, such as boundary layers, shock waves, and vortices, without leading to excessive computational cost. A mesh independence study was conducted to validate the mesh quality and ensure grid independence. The 2D model was employed with a rectangular structured mesh where elements were sized based on the edge lengths due to the selection of the free-face mesh.

(a) Without rib

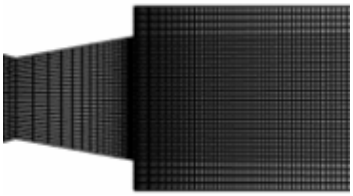

(b) Mesh closed up without rib

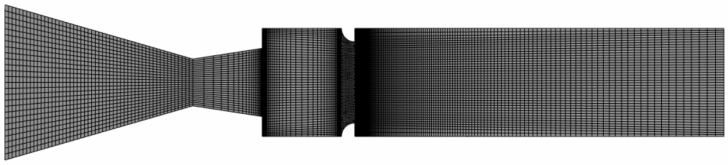

(c) With rib for orientation 1

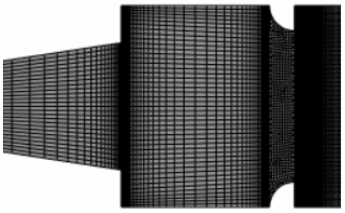

(d) Mesh closed up on with rib for orientation 1

Figure 3. Mesh model for mesh independence study.

Table 2. Boundary conditions of the design model

Zone	Geometry
Inlet	Nozzle inlet
Wall	Convergent-divergent nozzle wall
Base wall	Duct inlet
Axis	*x*-axis (axisymmetric line)
Rib	Rib wall
Outlet	Duct outlet

3.4. Assumptions and fluid properties

Assumptions are used to replicate the flow activities in the precise physical environment. Appropriate mathematical and numerical models are selected to make the governing equations.

To solve the governing equations simultaneously, numerical modeling requires selecting the appropriate mathematical models, including the governing equations, boundary conditions, mesh quality, and numerical method. Despite its limitations in accurately representing physical phenomena, the computational method has been trusted for decades and offers sufficient insight into flow behavior. As a result, this calls for careful consideration of elements that closely resemble the flow behavior. This study pinpoints the presumptions that jeopardize the precise physical state. The following are the presumptions and characteristics covered in this study:

(i) The flow is assumed to be a steady 2D flow because the geometry is symmetric.

(ii) The density of the air is variable.

(iii) Since turbulent flow has a significant impact on turbulent viscous dissipation at a given flow velocity, it is taken into consideration.

(iv) The viscosity of the fluid is dependent on the temperature.

(v) At the standard atmospheric pressure, the flows leave the duct. At normal ambient pressure, the flows leave the duct.

Since the flow via the nozzle is considered turbulent, the compressible flow field is represented by the k-ε standard model. The subsequent equations most appropriately characterize the turbulent flow.

3.5. Numerical and experimental results validation

The study initially involved replicating the experiment conducted by Rathakrishnan, in which five equidistant ribs were placed within a duct, as shown in Figure 4 (Rathakrishnan [29]), for method validation purposes. It also serves as a source of understanding the physics of the flow inside

the duct. Rathakrishnan's findings on the variation in base pressure with different NPR and L/D ratios, as shown in Table 3, served as a benchmark for comparison. Both controlled (with ribs) and uncontrolled (without ribs) flow configurations were simulated to ensure the accuracy of the numerical results.

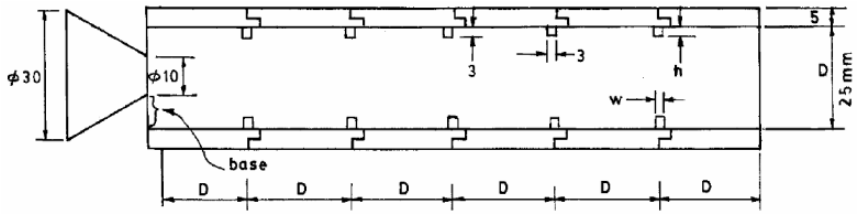

Figure 4. 2D simulation model of the Rathakrishnan's experimental study (Rathakrishnan [29]).

Table 3. Geometries of the validation model

Parameters	Dimensions
Nozzle inlet diameter	30 mm
Nozzle outlet diameter	10 mm
Converging nozzle length	20 mm
Duct diameter	25 mm
Duct length	Varies from 1D to 6D
Rib width	3 mm
Rib height	1 mm

A comparison between the numerical results and the previous Rathakrishnan's experimental data (Rathakrishnan [29]) was performed on a controlled model on ribs with an aspect ratio of 3:1. It was determined that for a duct with five 3:1 aspect ratio ribs, there was a good agreement as depicted in Figures 5(a) to (d). The percentage error was below 5%, ensuring the method's reliability. While isentropic flow theory suggests that sonic conditions should be achieved at the nozzle exit for a primary pressure ratio of 1.89, real-world flows are inherently viscous and non-isentropic. From this, minor discrepancies occur, which can be considered acceptable.

Moreover, the complex nature of compressible flow at sonic Mach numbers, characterized by shock waves and nonlinear behavior, can also contribute to slight variations in base pressure. Backflow and boundary layer effects at different L/D ratios may further influence these variations.

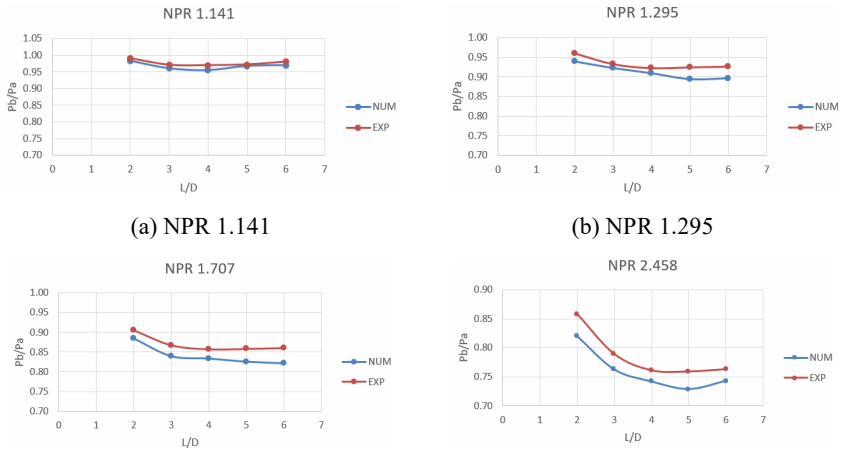

(a) NPR 1.141 (b) NPR 1.295

(c) NPR 1.707 (d) NPR 2.458

Figure 5. Graph of results validation at specific NPR.

3.6. Mesh independence study

The Mesh Independence Study (MIS) aims to determine the optimal mesh size for precise simulations that require shorter computational times without incurring excessive expenses. It considered multiple mesh configurations, ranging from coarsest to finest, with a progressive increase in the number of nodes and elements, as shown in Table 4. The node and element count were minimal in the coarsest mesh, reducing computational cost but leading to numerical diffusion and less accurate base pressure predictions. Flow separation and recirculation regions were not accurately captured, which affected the accuracy of the passive control analysis.

Table 4. Mesh independence study

Element size	Coarsest	Coarse	Medium	Fine	Finer	Finest
Nodes	3432	6452	15614	176755	553495	2508903
Elements	3271	6222	15148	175990	550097	2500485

As the mesh was refined to a medium level, the number of nodes and elements increased, improving the resolution of flow structures. Base pressure predictions became more stable, exhibiting less variation than those on the coarsest mesh. Flow separation and reattachment regions became more distinct, providing a better understanding of the passive control mechanism while minimizing computational cost. Further refinement led to a finer mesh, where velocity and pressure gradients were more accurately resolved. Base pressure predictions approached converged values with minimal variation compared to the medium mesh, ensuring reliable results. Flow structures, shock interactions, and turbulence effects were well captured, contributing to improved simulation accuracy.

The finest mesh contained the highest number of nodes and elements, but its results remained nearly identical to the fine mesh, confirming mesh independence. No substantial improvement in accuracy was observed, but the computational cost increased drastically.

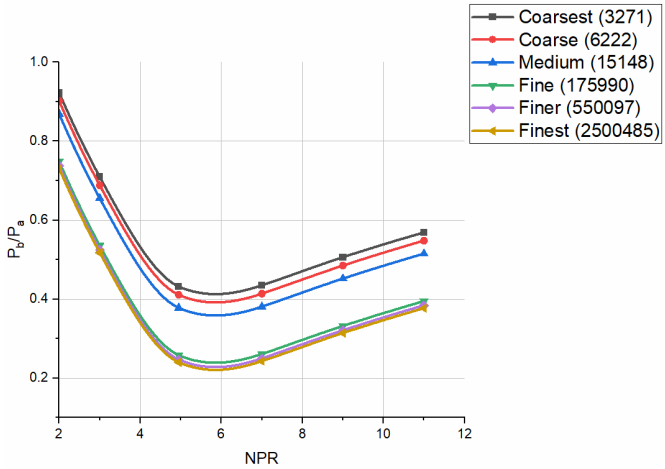

Figure 6. Results of mesh check.

The outcome of the MIS indicated that the base pressure converged beyond a certain refinement level, demonstrating that further mesh refinement did not significantly impact the results. The optimal mesh was selected based on a balance between accuracy and computational efficiency, typically favoring the fine or finer mesh, as illustrated in Figure 6.

4. Results and Discussion

Figures 7(a) to (d), respectively, show contour plots for pressure, velocity, temperature and turbulent kinetic energy without the control mechanism at $NPR = 3$. At this NPR, the jets are over-expanded, with a level of over-expansion indicated by $P_e/P_a = 0.61$. Figures 7(a) to (b) show the pressure and velocity inside the nozzle and the duct. There is also a pressure drop due to the sudden increase in the duct's cross-sectional area. Likewise, there is a maximum velocity in the diverging part of the nozzle; however, in the duct, the central part of the jet maintains the velocity. Still, near the duct wall, the velocity is low. Regarding the temperature distribution within the duct, there is a sudden decrease in temperature in the divergence part of the nozzle, as well as in the central part of the jet. Similarly, turbulent kinetic energy prevails in most of the duct; however, the value is low in the corners.

Contour plot without rib, $L/D = 6$

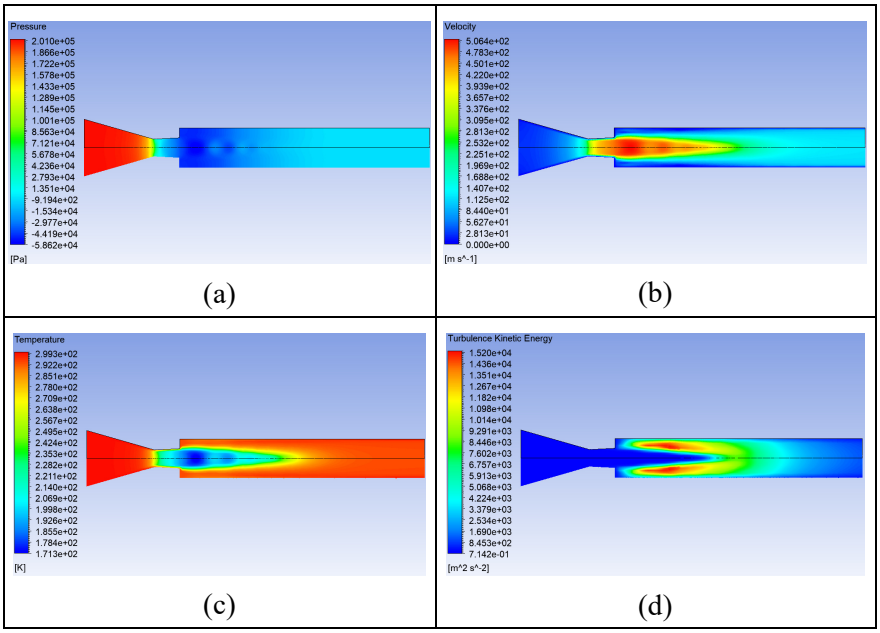

Figure 7. Contour plot for $L/D = 6$, without rib, and $NPR = 3$, where (a) pressure, (b) velocity, (c) temperature, and (d) turbulence kinetic energy.

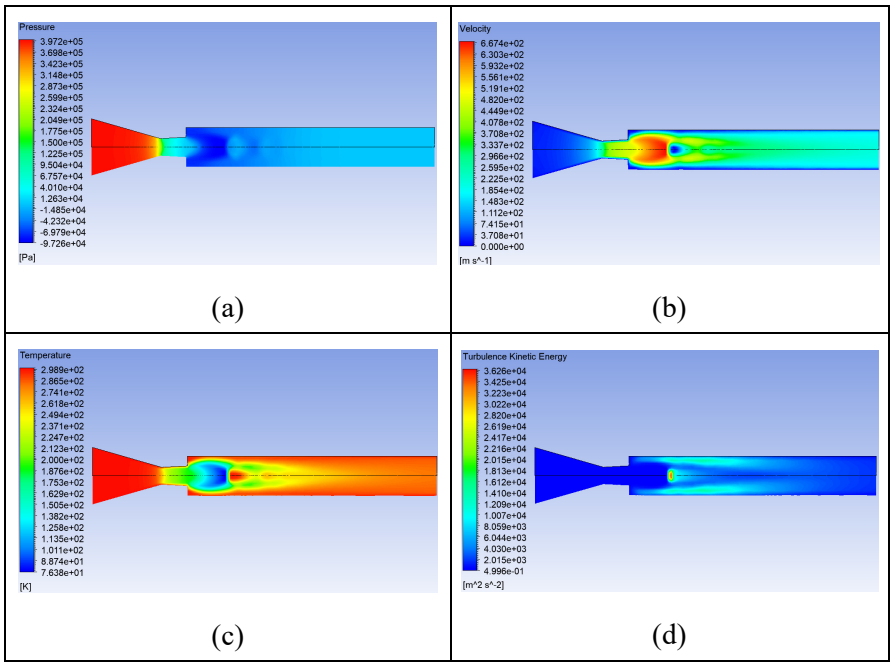

Figure 8. Contour plot for $L/D = 6$, without rib, and $NPR = 4.95$, where (a) pressure, (b) velocity, (c) temperature, and (d) turbulence kinetic energy.

Figures 8(a) to (d), respectively, show contour plots for pressure, velocity, temperature and turbulent kinetic energy without the control mechanism at $NPR = 4.94$. At this NPR, the jets are correctly expanded, and the level of expansion is $P_e/P_a = 1.0$. Figures 8(a) and (b), respectively, show the pressure and velocity inside the nozzle and the duct. There is a considerable pressure drop due to the sudden increase in the duct's cross-sectional area. Likewise, there is a maximum velocity in the diverging part of the nozzle; however, in the duct, most of the jet maintains its velocity, except near the wall, where low pressure is observed. Still, near the duct wall, the velocity is low. Regarding the temperature distribution in the duct, there is a sudden decrease in temperature in the divergence part of the nozzle and the central part of the jet over a small length, approximately $L/D = 1$. Similarly, low turbulent kinetic energy prevails in most of the duct; however, the value is low in the corners.

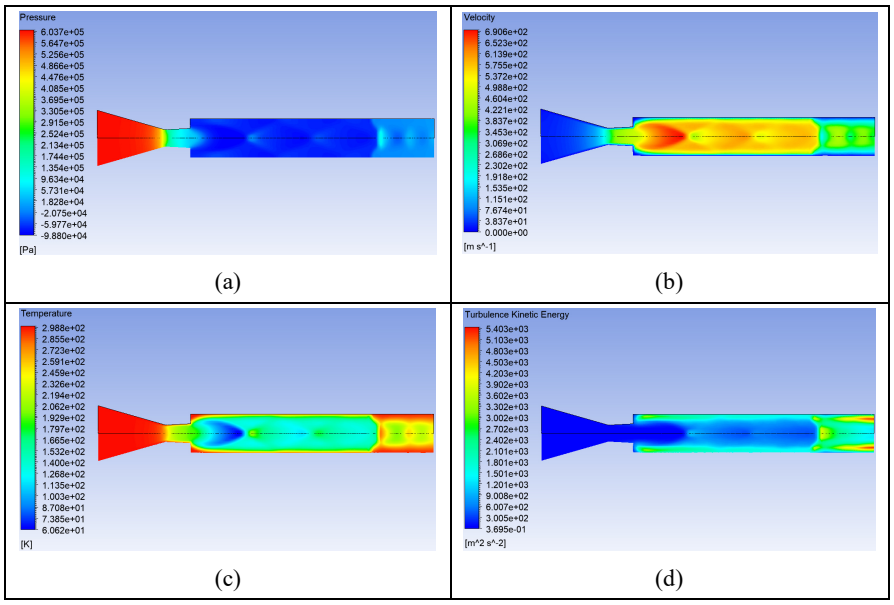

Figure 9. Contour plot for $L/D = 6$, without rib, and $NPR = 7$, where (a) pressure, (b) velocity, (c) temperature, and (d) turbulence kinetic energy.

Figures 9(a) to (d), respectively, show the pressure, velocity, temperature and turbulence kinetic energy in the duct at $NPR = 7$. At this $NPR = 7$, the nozzle is flowing under the influence of favorable pressure gradients. The effect of under-expansion is seen in Figure 9(a) of the duct. Similarly, the impact of under-expansion is seen in the velocity contour in Figure 9(b). Nearly seventy percent of the duct length maintains high velocity. A similar effect of under-expansion is observed in Figure 9(c) for the temperature in the duct resulting from the expansion of the flow. Seventy percent of the duct has a low temperature; however, the remaining thirty percent develops a high temperature near the wall. Similarly, we see the turbulence kinetic energy in Figure 9(d), which has attained a very low value; however, at the end of the duct, considerable increases in the turbulence energy are noticed.

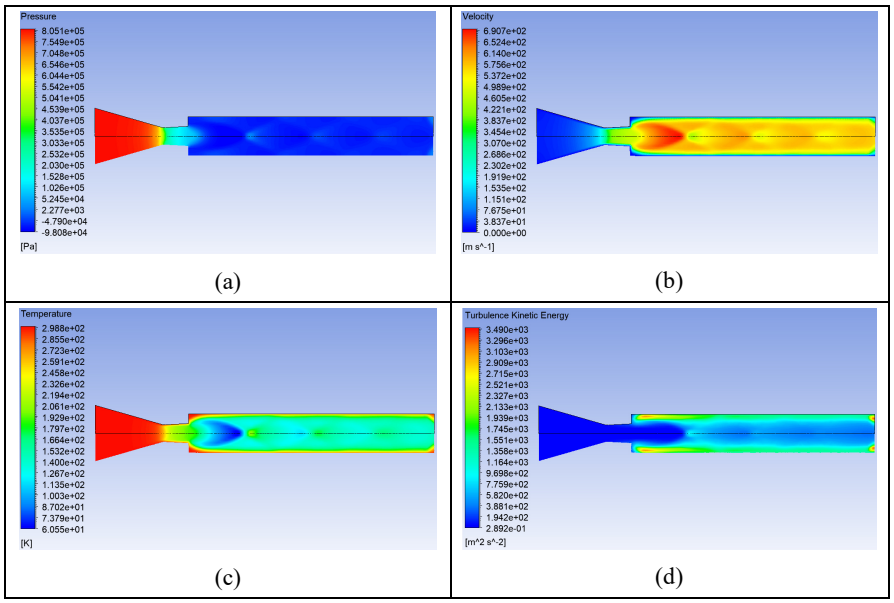

Figure 10. Contour plot for $L/D = 6$, without rib, and $NPR = 9$, where (a) pressure, (b) velocity, (c) temperature, and (d) turbulence kinetic energy.

Figures 10(a) to (d), respectively, show the pressure, velocity, temperature and turbulence kinetic energy in the duct at $NPR = 9$. At this $NPR = 9$, the nozzle is flowing under the influence of favorable pressure gradients. The effect of under-expansion is seen in Figure 10(a) of the duct. Similarly, the impact of under-expansion is seen in the velocity contour in Figure 10(b). Nearly 80% of the duct length maintains a high velocity. A similar effect of under-expansion is observed in Figure 10(c) for the temperature in the duct resulting from the expansion of the flow. Seventy percent of the duct has a low temperature; however, the remaining thirty percent develops a high temperature near the wall. Similarly, we see the turbulence kinetic energy in Figure 10(d), which has attained a very low value; however, at the end of the duct, considerable increases in the turbulence energy are noticed.

Base pressure analysis for rib orientation 1

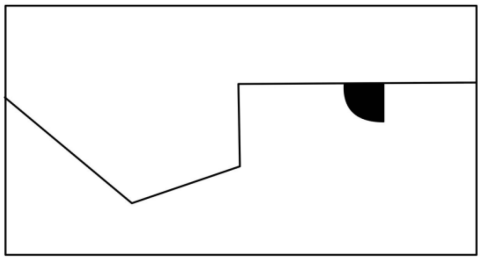

Figure 11. Nozzle and duct assembly with quarter rib as passive control for orientation 1.

Figure 11 shows the assembly of the converging-diverging nozzle and duct assembly with a quarter-circular rib in orientation 1. Simulations are conducted for both orientations, one and two. However, results are presented for orientation 1 in this section. For this case orientation, the rib's curved part will face the exiting flow from the nozzle.

4.1. Base pressure analysis for $L/D = 1$, orientation 1

Understanding the mechanics underlying the abruptly increased flow field would be helpful before interpreting the data. The nozzle exit boundary layer would grow as a free shear layer for subsonic flows and meet the immense duct wall downstream. The reattachment point is the position at which the flow attaches. The reattachment length is the distance from the base to the point of reattachment. One or more vortices will be positioned between the reattachment point, the base, and the free shear layer edge; the primary vortex is the initial, more powerful one closest to the base. That pumps fluid from the base to the main flow on the other side of the free shear layer edge. At the base, low pressure is the result of this pumping motion. However, the pumping also becomes periodic because vortex shedding is a periodic phenomenon. As a result, there are variations in the base pressure. The base pressure fluctuations, however, were frequently found to be tiny and could be expressed as a mean value. The periodicity of the vortex motion causes the entire flow field in the duct to oscillate. The

oscillations can become severe for certain combinations of geometrical factors and flow.

The flow Mach number and the reattachment control the primary vortex strength, which also significantly impacts the amount of suction at the base and the flow oscillations in the duct. Depending on whether the flow is overexpanded or underexpanded, an oblique shock ring or an expansion fan ring is located at the nozzle outlet for supersonic Mach numbers. The flow accelerates and veers off when there is an expansion. Early reattachment and shorter reattachment length will result from this additional turning, as well as the turning caused by free expansion. When an oblique shock occurs, the flow is directed toward the duct centerline, which delays and lengthens the reattachment process. Therefore, the waves will significantly impact strength in any scenario since the base pressure and flow field oscillations depend on the primary vortex. The flow will encounter more vortices shed at the rib if the duct has annular ribs. The base pressure may rise due to these smaller vortices acting as promoters of mixing.

Base pressure results for duct length $L/D = 1$ and rib location of $L/D = 0.5$ for various expansion levels are shown in Figure 12. From the figure, it is seen that there is a decrease in the base pressure until $NPR = 7.5,$ and later there is an increase in the base pressure for the case without control. The physics behind the trend is that the base pressure will decrease as long as the nozzle is over-expanded. However, once the nozzle flows under the influence of favorable pressure gradients, the base pressure increases. In this case, the NPR required for correct expansion is approximately 5, but the base pressure increases significantly beyond the NPR needed for ideal expansion. The reason for this trend may be as follows. The physics behind this trend may be that when the relief effect due to the increase in the area ratio exceeds a specific limit, the flow from the nozzle discharged into the enlarged duct tends to reattach with a reattachment length other than the optimum for a strong vortex at the base. This process makes the NPR effect on base pressure insignificant for a

higher area ratio. That may be why the shift of NPR from 5 to 7.5 is due to the increase in the area ratio, which is 4 in this case. When passive control is employed at $L/D = 0.5$ and rib radii are 1.5 mm, 2 mm, and 3 mm, the results indicate that rib radii 1.5 mm and 2 mm become effective from $NPR = 7,$ and the base pressure ratios are 0.75 and 0.9.

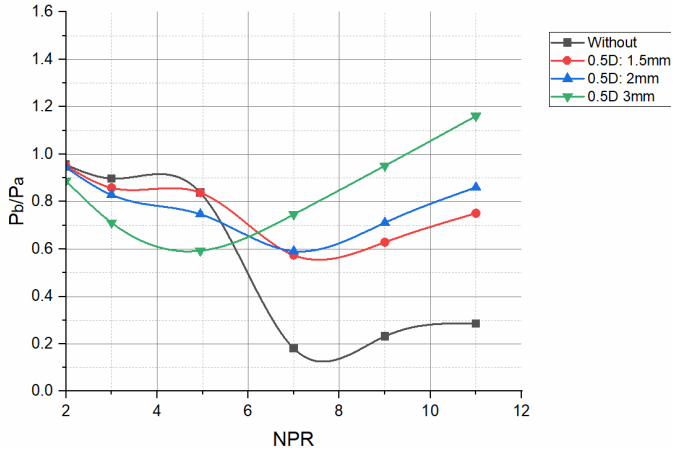

Figure 12. Base pressure vs. NPR for various rib sizes at $L/D = 0.5$ location for $L/D = 1$.

Meanwhile, for the highest rib radius of 3 mm, the base pressure ratio is 1.2, and a decreasing trend in the base pressure is reversed at $NPR = 5,$ which is the NPR required for ideal expansion. Therefore, these results reiterate that the active or passive control mechanism will become effective once the nozzles are correctly expanded or under-expanded. Results show the oscillatory nature of the flow; it may be due to the location of the rib being at $L/D = 0.5,$ and for this rib location, the shear layer exiting from the nozzle is still in transition and has not settled; hence, these results may give a trend, but the flow has not settled and needs more duct length to get stabilized. Another critical point is that for an L/D ratio of one, the back pressure will have the maximum influence. This short duct length may not reveal a definite trend in the flow pattern.

4.2. Base pressure analysis for $L/D = 2$, orientation 1

Figure 13 depicts the outcomes of the present study for duct length of 2D for various rib locations at $L/D = 0.5, 1,$ and 1.5 for rib radius 1.5 mm and 3 mm for NPRs in the range 2 to 11. The figure shows that in the absence of the control, the decreasing trend in the base pressure is reversed at $NPR = 7,$ which is slightly more than the NPR required for ideal expansion. This trend is attributed to the duct diameter and the relief available to the flow when the control mechanism is employed at $L/D = 0.5, 1.0,$ and 1.5, and ribs with 1.5 mm and 3 mm. For rib locations at $L/D = 0.5$ with a rib radius of 1.5 mm, it becomes effective for $NPR > 5,$ which is the NPR required for ideal expansion. There is a progressive increase in the base pressure, with a base pressure ratio of 0.8. However, when ribs of radius 1.5 mm are placed at $L/D = 1.0$ and 1.5, the former is unable to regulate the base pressure. When the nozzle is highly under-expanded, with NPR above 7, the control results in a decrease in base pressure.

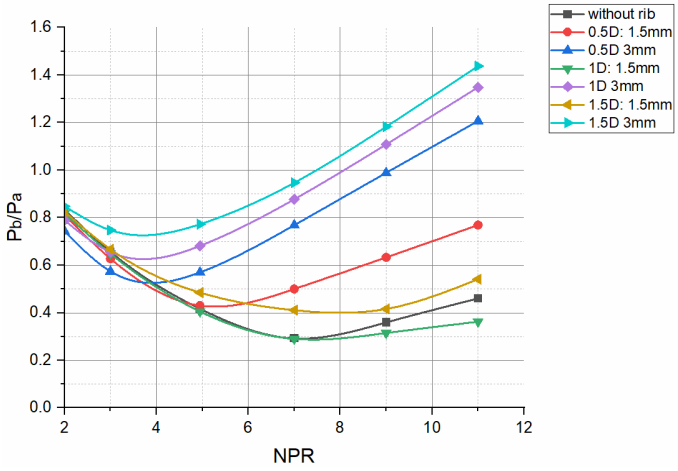

Figure 13. Base pressure vs. NPR for various rib sizes at different locations for $L/D = 2$.

In contrast, for rib location $L/D = 1.5,$ right from $NPR = 3$ and above, there is an increase in the base pressure; however, the base pressure ratio

remains at 0.55. This phenomenon can be understood by examining the shock patterns at the nozzle exit and the subsequent separation of the shear layer, as well as the interaction between the base vortex and the secondary vortices formed due to the presence of the rib. Also, these waves will hit the duct wall and get reflected. The 3 mm rib radius results differ from the 1.5 mm rib radius for the exact rib locations. As we consider the orientation of the rib where the curved part interacts with the shear flow, the curved part of the rib will exhibit a gradual variation in flow properties rather than a sudden variation in flow parameters. In the case of the largest rib radius, the ribs block flow, increasing the base pressure.

4.3. Base pressure analysis for $L/D = 3$, orientation 1

Figure 14 presents the findings of the present study. The base pressure is presented as a function of NPR for a given rib location and the rib radius for a duct $L/D = 3$, while the curved part faces the flow exiting from the CD nozzle at Mach 1.7. The rib locations considered were $L/D = 0.5$, 1.0, 1.5, and 2.0. Based on the rib radius, there are two sets of results: one for 1.5 mm and another for 3 mm. The figure shows that the rib radius is 1.5 mm and 3 mm, and the corresponding values of the base pressure ratios (P_b/P_a) are 0.8, 0.4, 0.61, and 0.5. It is seen that the pattern of the effectiveness of the rib locations in descending order is $L/D = 0.5$, 1.5, 2.0, and 1.0. The physics behind this pattern is that when the rib radius is 1.5 mm and located at $L/D = 0.5$, the secondary vortices created interact with the base vortices and become most effective when nearest to the recirculation zone. For the remaining locations, the base pressure values will depend on the reattachment point, reattachment length, and interactions between the vortices created by the presence of the rib, among other factors. In this case, the rib locations do not exhibit a definite trend due to the small rib radius and the varying shock strengths.

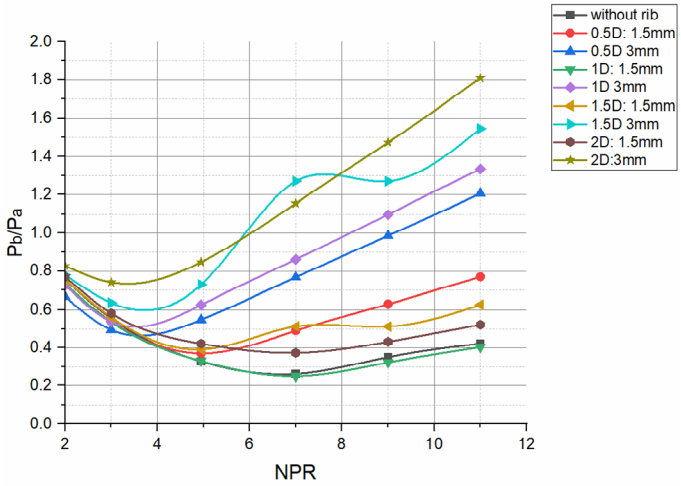

Figure 14. Base pressure vs. NPR for various rib sizes at various locations for $L/D = 3$.

When we look at the base pressure results for the 3 mm rib radius, the base pressure ratios for the various rib locations are 1.8, 1.58, 1.35, and 1.2 for rib locations at $L/D = 2.0,\ 1.5,\ 1.0,$ and 0.5, respectively. For the rib radius of 3 mm, there is a progressive increase in the base pressure with the shift in the rib locations towards the downstream, except for the rib location at $L/D = 1.5$. The physics of the flow for such an oscillatory pattern in the base pressure values may be related to the reattachment point, which is expected to be located somewhere between $L/D = 1.0$ and 2.0. When the rib is located near the reattachment point, the flow field in the duct will become oscillatory due to the presence of the rib as a passive control mechanism.

4.4. Base pressure analysis for $L/D = 4$, orientation 1

The outcomes of this study are displayed in Figure 15, the normalized base pressure ratio as a function of nozzle pressure ratio ranging from 3 to 11 for rib placement at $L/D = 0.5,\ 1.0, 1.5, 2.0,$ and 3.0 for rib radii 1.5 mm and 3 mm for the duct length to diameter ratio of 4 (i.e., $L/D = 4$). The

results indicate that their values are similar to the $L/D = 3$, except for rib placement, where the rib is located at $L/D = 3$. For $L/D = 3$ rib placement, the base pressure ratio is 2.2 for a rib radius of 3 mm. When we analyze the results for a rib radius of 1.5 mm, the results are similar to those for an L/D ratio of 3 and a duct length. For a rib radius of 1.5 mm, when placed at $L/D = 3$, there is no significant difference in the base pressure, and its values are similar to the rib location at $L/D = 1.5$. This indicates that the shift of the rib, with a radius of 1.5 mm, does not alter the base pressure, as the secondary vortices generated by its presence cannot displace additional mass toward the base region. Hence, there is no significant change in the base.

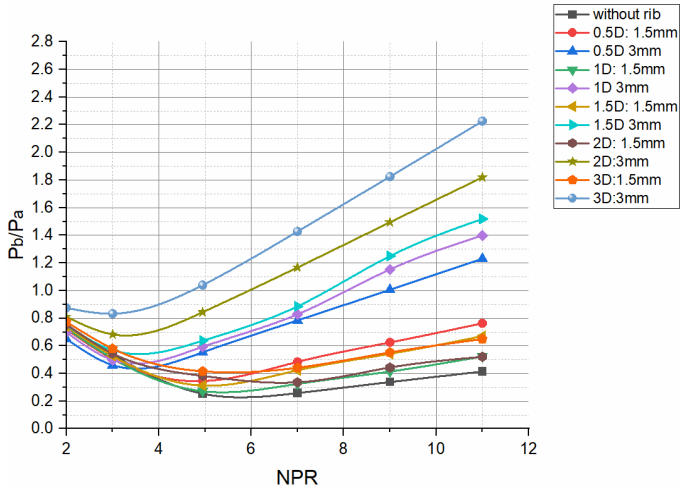

Figure 15. Base pressure vs. NPR for various rib sizes at various locations for $L/D = 4$.

4.5. Base pressure analysis for $L/D = 5$, orientation 1

Figure 16 presents the base pressure results from the present study and their dependence on NPR for a duct L/D ratio of 5, with two rib radii: 1.5 mm and 3 mm, and for rib locations at $L/D = 0.5$, 1.0, 1.5, 2.0, and 3.0. As previously discussed, the results exhibit two distinct patterns. For a

rib radius of 3 mm, when employed, there is a consistent increase in base pressure when the rib is placed at different locations inside the duct. The base pressure ratio increases from 0.4 (without control) to 1.2 to 2.2. In contrast to the rib radius of 1.5 mm, for similar rib locations where there is an increase in base pressure, the increase in base pressure does not exhibit a definite pattern. The reason for this trend is the same as discussed earlier: this small rib radius cannot influence the flow field in the separated region compared to the case where the rib radius is 3 mm. The base pressure values are nearly the same for both the radius and the locations, except for marginal changes due to variations in duct lengths and the influence of backpressure.

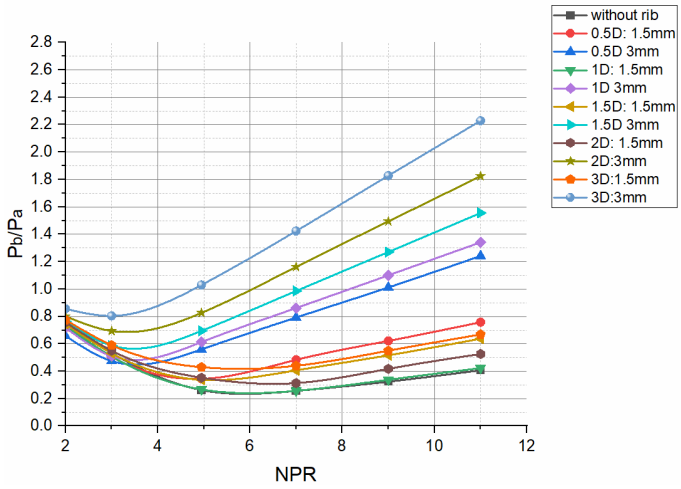

Figure 16. Base pressure vs. NPR for various rib sizes at various locations for $L/D = 5$.

4.6. Base pressure analysis for $L/D = 6$, orientation 1

Figure 17 shows similar results for the highest duct length, with an L/D ratio of 6, while maintaining the same rib radius and locations. According to the findings of this study, a rib radius of 3 mm results in an appreciable increase in base pressure for a rib location with $L/D = 3$. There are marginal changes in the base pressure values for the remaining rib locations.

The base pressure pattern for rib radius 1.5 mm for similar rib locations remains the same. Therefore, if the mission requirements are to decrease the base suction by fifty percent, then a rib radius of 1.5 mm is the right choice. The exact rib location can be fixed based on the user's need to the extent that they want to increase the base pressure. In contrast, the 3 mm rib radius will be employed when we are interested in improving the base pressure of the manifold to the ambient atmospheric pressure. Hence, it may be concluded that the rib radius and their locations are case-sensitive, and one has to decide based on the user's requirements.

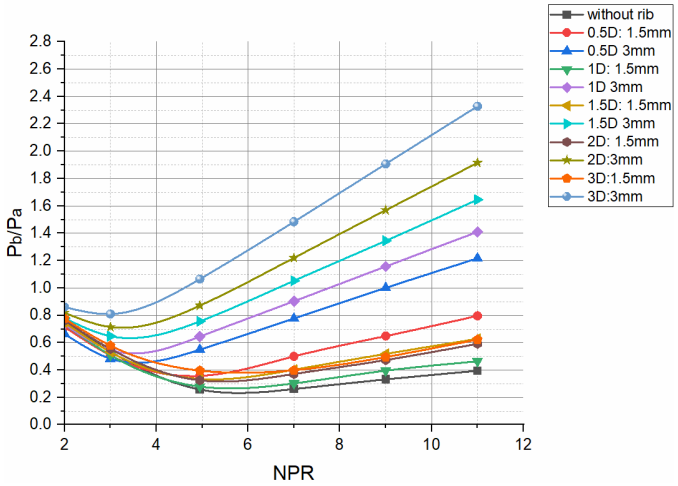

Figure 17. Base pressure vs. NPR for various rib sizes at various locations for $L/D = 6$.

4.7. Contour plot for $L/D = 6$ at 1D location, orientation 1

Figures 18(a) to (d), respectively, show the pressure, velocity, temperature, and turbulence kinetic energy at $NPR = 3$. Since the nozzle is over-expanded and the rib radius is 1 mm, there is no appreciable change in these parameters, and they exhibit nearly identical patterns, as discussed earlier.

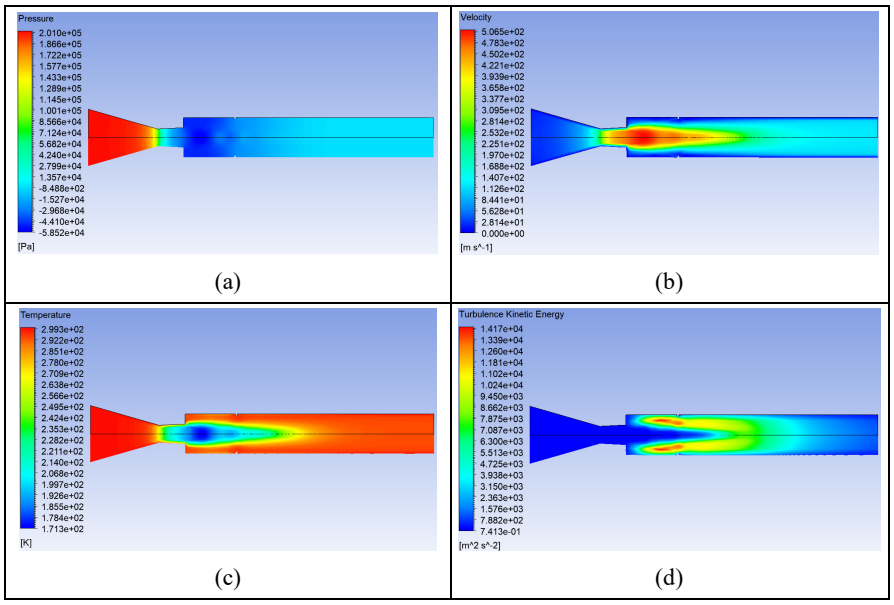

Figure 18. Contour plot for $L/D = 6$, 1 mm rib, and $NPR = 3$, where (a) pressure, (b) velocity, (c) temperature, and (d) turbulence kinetic energy.

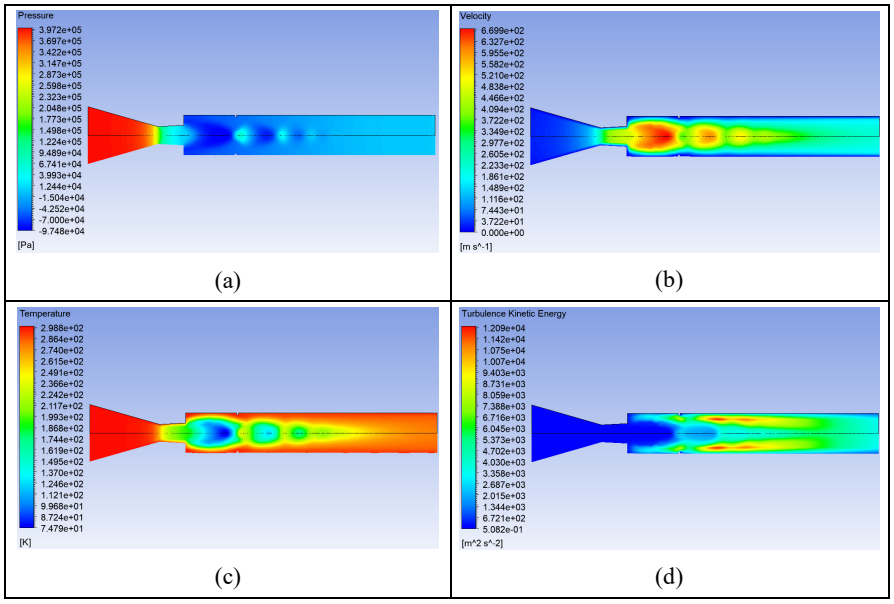

Figure 19. Contour plot for $L/D = 6$, 1 mm rib, and $NPR = 4.95$, where (a) pressure, (b) velocity, (c) temperature, and (d) turbulence kinetic energy.

Figures 19(a) to (d), respectively, show the contours for pressure, velocity, temperature, and turbulence kinetic energy. In Figure 19(a), as the flow is perfectly expanded, Mach waves form, and due to the increase in duct area, this results in low pressure. As far as velocity is concerned, low values are just near the wall. Still, fifty percent of the duct's length has high velocity. The temperature in the diverging part of the nozzle attains low values, and this trend continues till forty percent of the duct. Later, the temperature recovers. Similarly, the turbulence kinetic energy also has low values due to the nozzle being perfectly expanded; however, beyond fifty percent of the duct's length, turbulence kinetic energy recovers.

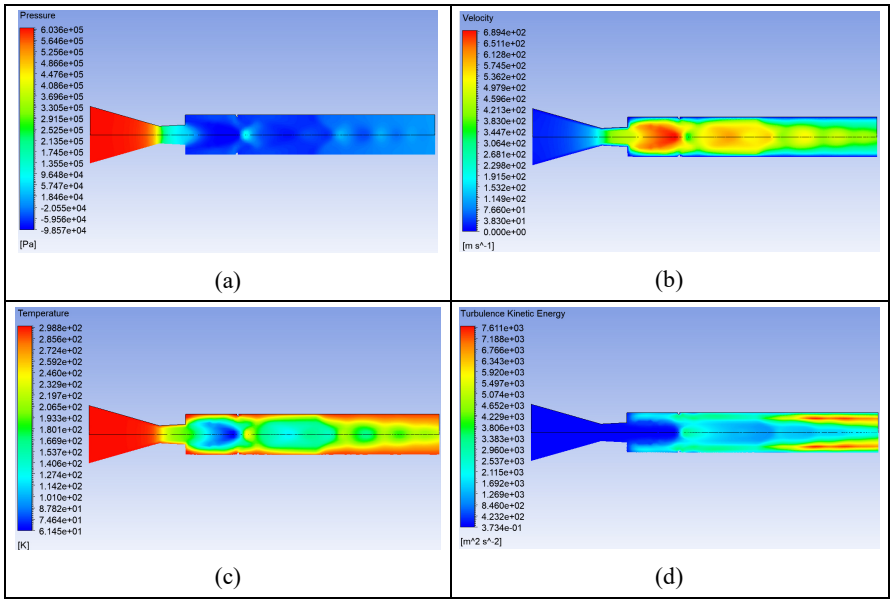

Figure 20. Contour plot for $L/D = 6$, 1 mm rib, and $NPR = 7$, where (a) pressure, (b) velocity, (c) temperature, and (d) turbulence kinetic energy.

Figures 20(a) to (d), respectively, show the contours for pressure, velocity, temperature, and turbulence kinetic energy. In Figure 20(a), the nozzle is under-expanded. At a level of under-expansion of 1.42 (i.e., $P_e/P_a = 1.42$), an expansion fan will be present, and the flow will expand beyond being exhausted into a larger space. That will cause a decrease in pressure inside the duct, as is evident in the results. As far as

velocity is concerned, low values are just near the wall. Still, ninety percent of the duct's length has high velocity. The temperature in the diverging part of the nozzle attains low values, and this trend continues till ninety percent of the duct. Later, the temperature recovers. Similarly, the turbulence kinetic energy also has low values due to the nozzle being under-expanded. This condition persists until beyond seventy percent of the duct length, where turbulence kinetic energy recovery occurs.

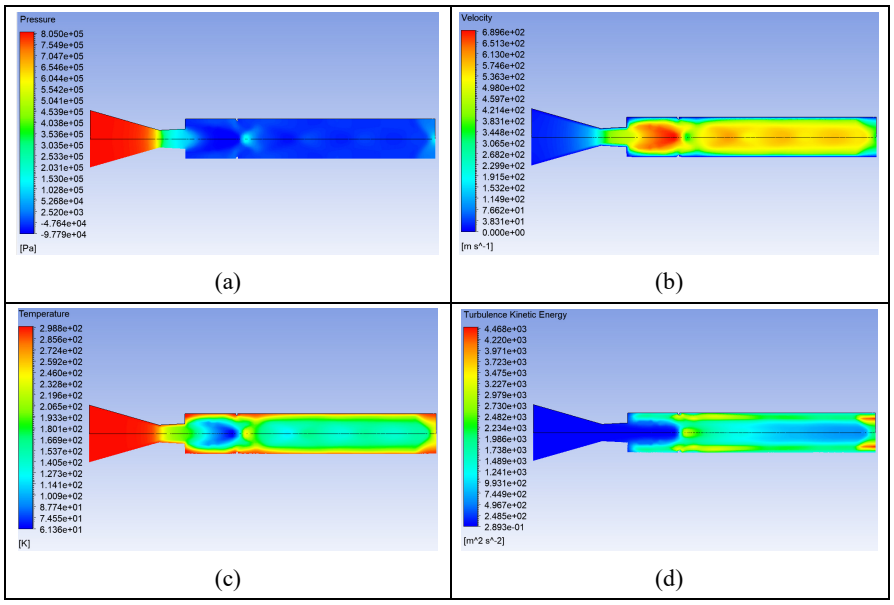

Figure 21. Contour plot for $L/D = 6$, 1 mm rib, and $NPR = 9$, where (a) pressure, (b) velocity, (c) temperature, and (d) turbulence kinetic energy.

Figures 21(a) to (d), respectively, show the contours for pressure, velocity, temperature, and turbulence kinetic energy at $NPR = 9$ when a 1 mm rib radius is placed. In this case, NPR has further increased, resulting in a higher level of under-expansion. In Figure 21(a), as this is under-expanded and the level of under-expansion is 1.82 (i.e., $P_e/P_a = 1.82$), the increased level of under-expansion will result in high velocity inside the duct. The length of the duct has high velocity. The temperature in the diverging part of the nozzle attains low values, and this trend continues till ninety percent of the duct. Later, the temperature recovers. Similarly, the

turbulence kinetic energy also has low values due to the nozzle being under-expanded. This condition persists until beyond seventy percent of the duct length, where turbulence kinetic energy recovery occurs.

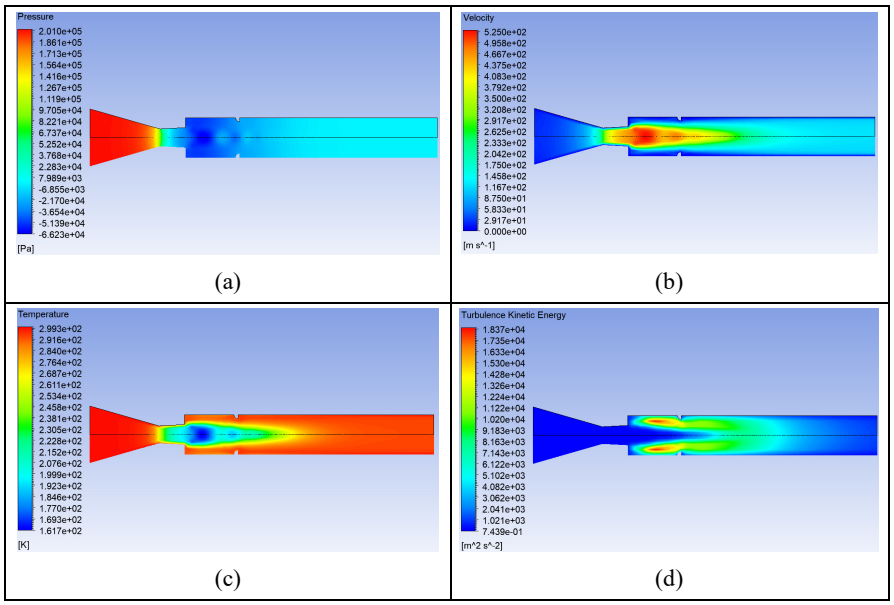

Figure 22. Contour plot for $L/D = 6$, 2 mm rib, and $NPR = 3$, where (a) pressure, (b) velocity, (c) temperature, and (d) turbulence kinetic energy.

Figures 22(a) to (d), respectively, show the contours for pressure, velocity, temperature, and turbulence kinetic energy for $L/D = 6$, $NPR = 3$, and 2 mm rib radius. In Figure 22(a), as this is over-expanded and the level of under-expansion is 0.61 (i.e., $P_e/P_a = 0.61$), there will be an oblique shock wave. The pressure increases until it becomes equal to the ambient pressure, apart from being exhausted into a larger area, which causes a decrease in the pressure inside the duct, as shown in the figure. As far as velocity is concerned, low values are just near the wall. Still, forty percent of the duct's length has high velocity. The temperature in the diverging part of the nozzle attains low values, and this trend continues till forty percent in the central part of the duct. Later, the temperature recovers. Similarly, the turbulence kinetic energy also has low values due to the nozzle

being over-expanded. This condition persists until beyond forty percent of the duct length, where turbulence kinetic energy recovery occurs.

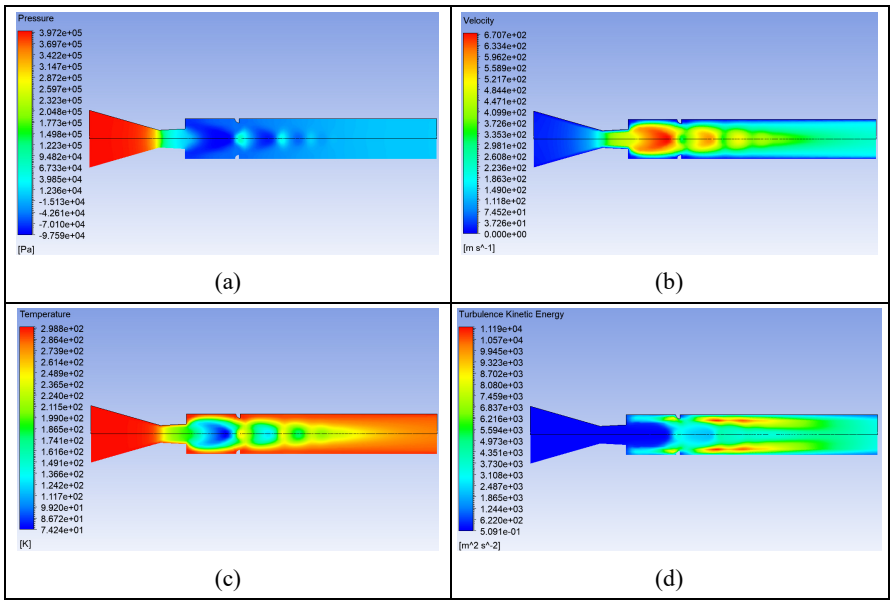

Figure 23. Contour plot for $L/D = 6$, 2 mm rib, and $NPR = 4.95$, where (a) pressure, (b) velocity, (c) temperature, and (d) turbulence kinetic energy.

Figure 23 shows similar results for $L/D = 6$, rib radius = 2 mm, and $NPR = 4.94$. Figure 23(a) shows a pressure contour that extends beyond the rib location as the duct expands correctly, forming Mach waves rather than oblique shock waves or expansion fans. Due to the sudden increase in the area, the velocity assumes low values near the wall; however, the primary jet contains high kinetic energy. Similarly, the assumption is that low values are in the initial part of the duct and the primary jet. As far as the turbulent kinetic energy is concerned, its value is low inside the nozzle and remains constant for the majority of the length until approximately twenty percent.

Figure 24 shows similar results for $NPR = 7$, with all other parameters remaining the same. This figure reflects the effect of expansion levels. As the nozzle is under-expanded, the flow will further expand through the

expansion fan; hence, a low-pressure contour is seen in Figure 24(a). Similarly, the velocity contour shows the increase in the velocity in the duct (Figure 24(b)). Likewise, the temperature takes lower values, as seen in Figure 24(c). Lastly, the turbulent intensity assumes lower values for short duct lengths but later increases.

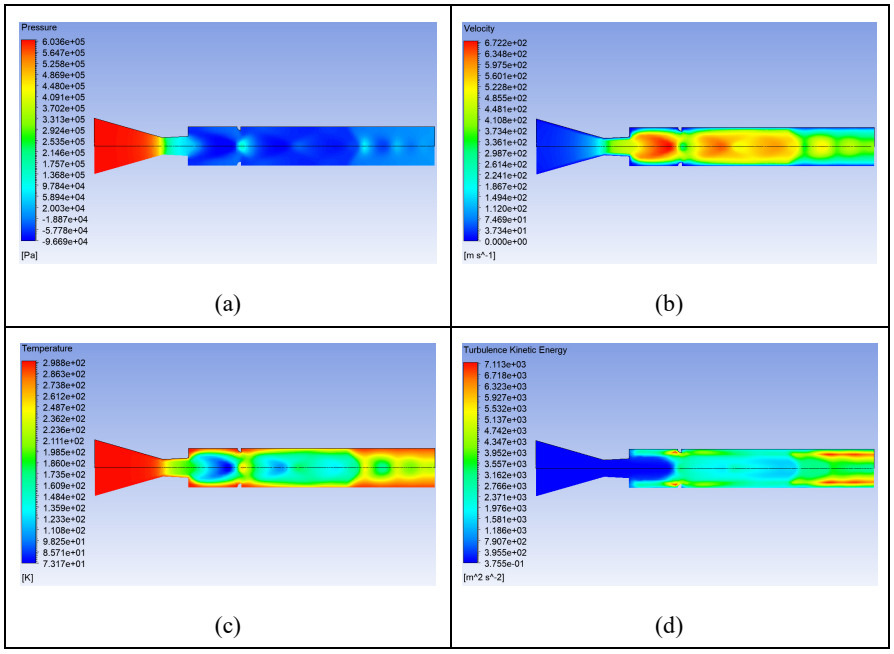

Figure 24. Contour plot for $L/D = 6$, 2 mm rib, and $NPR = 7$, where (a) pressure, (b) velocity, (c) temperature, and (d) turbulence kinetic energy.

Similar results are observed for pressure, velocity, temperature, and turbulent intensity, as shown in Figure 25 for $NPR = 7$. The only difference in this figure is that the NPR has increased from 7 to 9, and hence, the level of expansion has increased from 1.42 to 1.82.

Similar results for $L/D = 6$, 2 mm rib radius, and NPR 9 are shown in Figures 25(a) to (d).

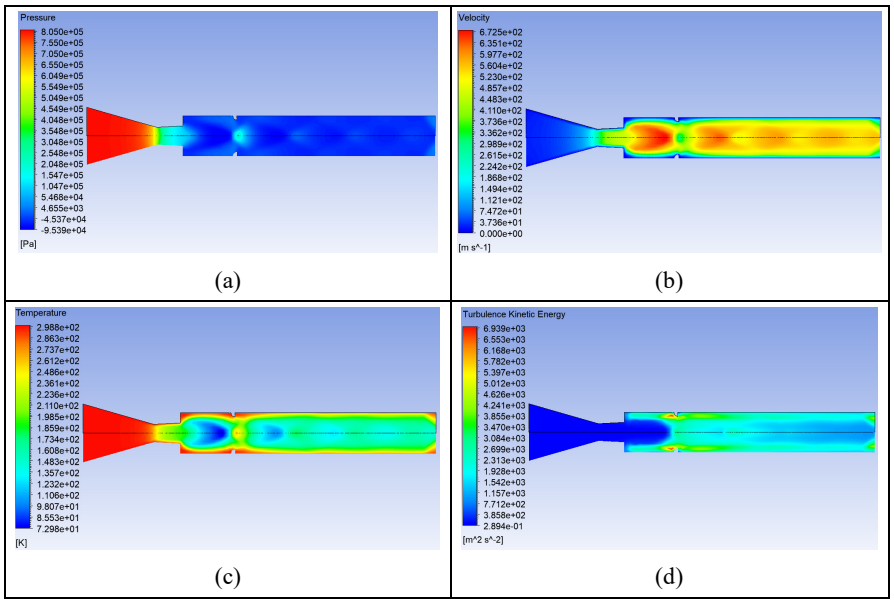

Figure 25. Contour plot for $L/D = 6$, 2 mm rib, and $NPR = 9$, where (a) pressure, (b) velocity, (c) temperature, and (d) turbulence kinetic energy.

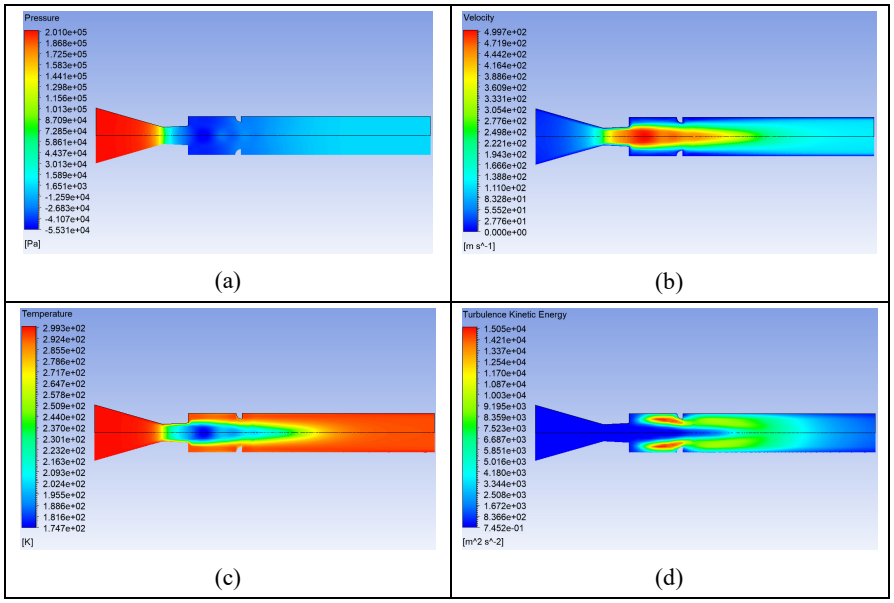

Figure 26. Contour plot for $L/D = 6$, 3 mm rib, and $NPR = 3$, where (a) pressure, (b) velocity, (c) temperature, and (d) turbulence kinetic energy.

Figure 26 shows the contours of pressure, velocity, temperature, and turbulence kinetic energy for $L/D = 6$, rib radius = 3 mm, and $NPR = 3$. Here, the nozzle is over-expanded. Due to the rise in the rib radius, the flow exiting from the nozzle will encounter the rib of maximum radius and block the flow. Accordingly, the pressure, velocity, temperature, and turbulence kinetic energy will be modified.

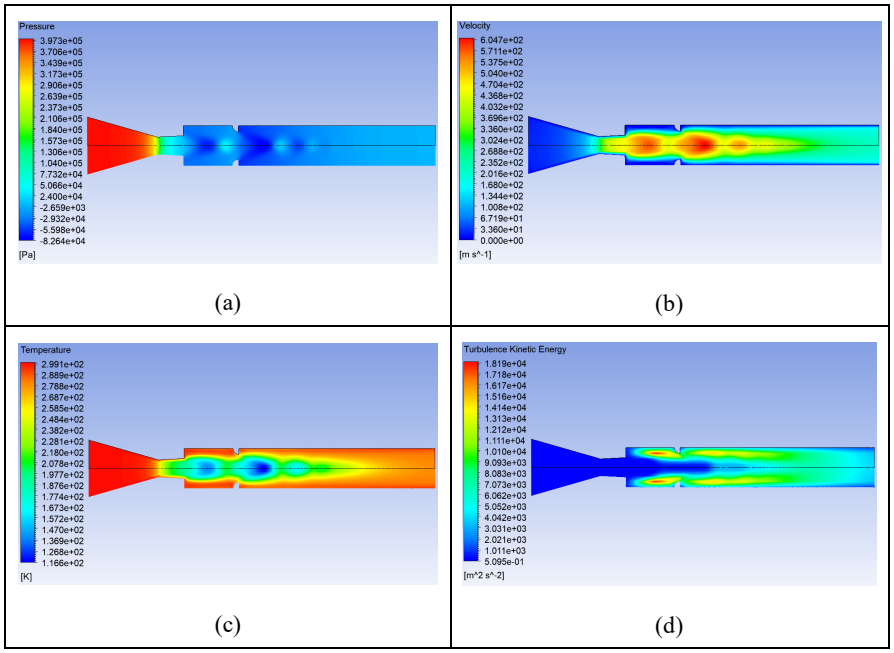

Figure 27. Contour plot for $L/D = 6$, 3 mm rib, and $NPR = 4.95$, where (a) pressure, (b) velocity, (c) temperature, and (d) turbulence kinetic energy.

Figure 27 shows the results of pressure, velocity, temperature, and kinetic energy for the ideally expanded nozzle. Here, due to the presence of the Mach waves, we will have marginal changes in the flow parameters.

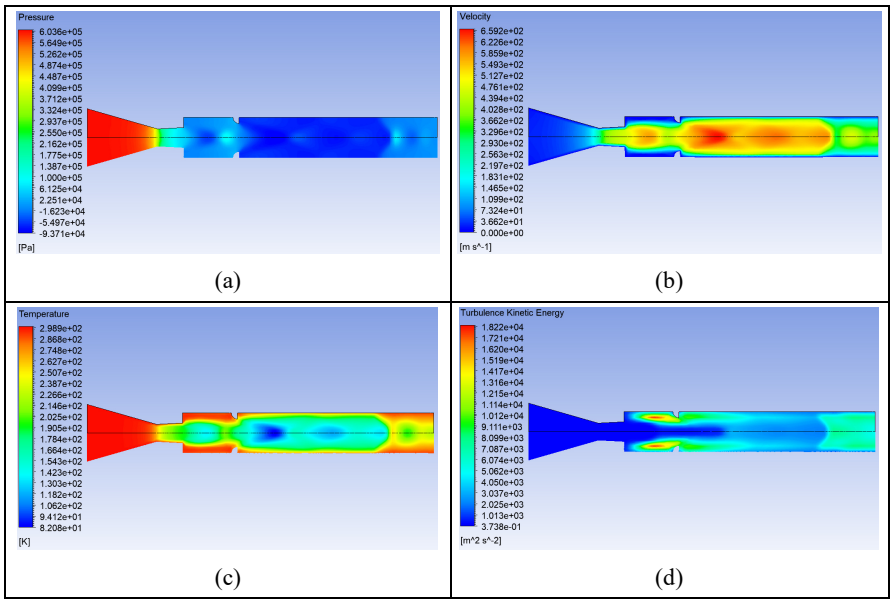

Figure 28. Contour plot for $L/D = 6$, 3 mm rib, and $NPR = 7$, where (a) pressure, (b) velocity, (c) temperature, and (d) turbulence kinetic energy.

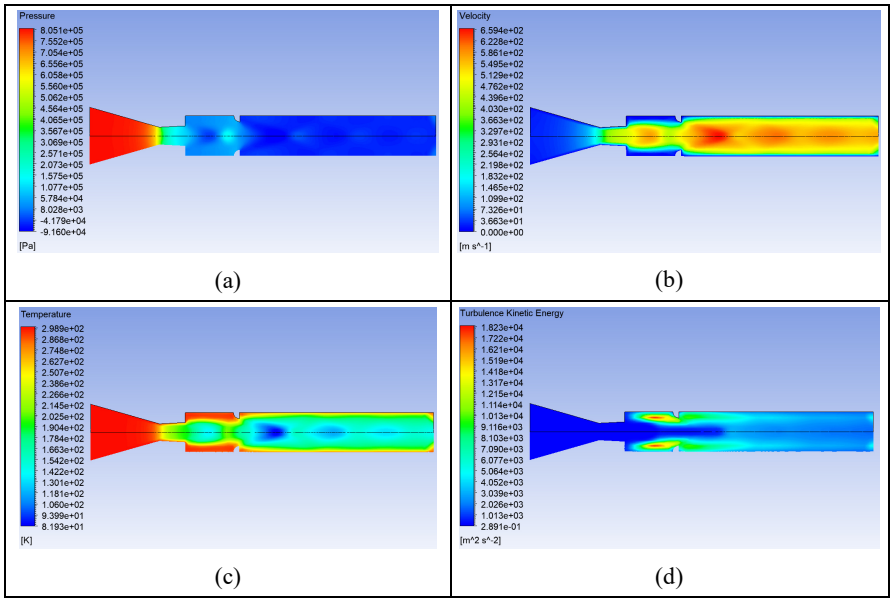

Figure 29. Contour plot for $L/D = 6$, 3 mm rib, and $NPR = 9$, where (a) pressure, (b) velocity, (c) temperature, and (d) turbulence kinetic energy.

Figures 28 to 29 show similar results for an increase in NPR values of 7 and 9, where the jet undergoes an expansion resulting in lower pressure, high velocity, low temperature, and high kinetic energy.

5. Conclusions

This study investigates the passive control of base pressure at a supersonic Mach number $(M = 1.7)$ for an area ratio of 4, using quarter ribs. It analyzes the effects of rib size, rib location, nozzle pressure ratio (NPR), and rib orientation. The findings demonstrate that the introduction of ribs has a significant influence on shear layer interactions, resulting in variations in base pressure that depend on rib size, placement, and orientation. The rib with a 1.5 mm radius increases base pressure by 50%, equivalent to the back pressure. Additionally, a 3 mm rib increases base pressure by 240%, making it ideal for applications that require a base pressure higher than the ambient pressure. Subsequently, passive control proves highly effective in reducing suction within the recirculation zone when a 3 mm rib is positioned at $L/D = 2$ or 3.0.

Furthermore, rib location also plays a crucial role in influencing base pressure recovery. There is a mixed trend for rib radius 1.5 mm when placed at different locations. The rib size cannot decrease the base suction in the recirculation zone. However, the small rib radius has increased the base pressure ratio from 0.4 to 0.8, and the base pressure ratio for a rib radius of 3 mm has risen from 1.2 to 2.4.

The study further establishes that variations in duct length do not introduce significant changes in base pressure trends, reaffirming that the primary factors governing flow behavior are the rib's geometric properties and its interaction with the shear layer. However, at $L = 0.5D$, flow oscillations are observed due to its proximity to the nozzle exit, where the shear layer remains in a transitional state before stable reattachment occurs. Ultimately, these results serve as a technological demonstration, highlighting the importance of selecting an appropriate combination of parameters to meet specific mission requirements.

Future studies can focus on enhancing accuracy by implementing advanced turbulence models to more accurately predict flow separation and vortex dynamics. Moreover, exploring hybrid control strategies that combine passive methods with active techniques, such as micro-jets or plasma actuators, could further enhance pressure recovery and reduce drag, leading to more efficient aerodynamic systems. Machine learning techniques can be integrated to optimize rib configurations and predict base pressure variations under different conditions.

References

[1] A. Khan, P. Rajendran, J. S. S. Sidhu and M. Sharifpur, Experimental investigation of suddenly expanded flow at sonic and supersonic Mach numbers using semi-circular ribs: a comparative study between experimental, single layer, deep neural network (SLNN and DNN) models, European Physical Journal Plus 138(4) (2023), 314. https://doi.org/10.1140/epjp/s13360-023-03853-1.

[2] A. Khan, N. M. Mazlan and E. Sulaeman, Effect of ribs as passive control on base pressure at sonic Mach numbers, CFD Letters 14(1) (2022), 140-151. https://doi.org/10.37934/cfdl.14.1.140151.

[3] A. Khan, S. A. Khan, V. Raja, A. Aabid and M. Baig, Effect of ribs in a suddenly expanded flow at sonic Mach number, Heliyon 10(9) (2024), e30313. https://doi.org/10.1016/j.heliyon.2024.e30313.

[4] A. Khan, N. M. Mazlan and M. A. Ismail, Numerical simulation of suddenly expanded flow from converging nozzle at sonic Mach number, Lecture Notes in Mechanical Engineering, 2020, pp. 349-359. https://doi.org/10.1007/978-981-15-4756-0_29.

[5] A. Khan, M. N. Akhtar, A. Aabid, M. Baig and S. A. Khan, Comprehensive CFD analysis of base pressure control using quarter ribs in sudden expansion duct at sonic Mach numbers, International Journal of Thermofluids 24 (2024), 100908. https://doi.org/10.1016/j.ijft.2024.100908.

[6] A. Khan, M. N. Akhtar, S. A. Khan, A. Aabid and M. Baig, Base pressure control with semi-circular ribs at critical Mach number, Fluid Dynamics and Materials Processing 20(9) (2024), 2007-2028. https://doi.org/10.32604/fdmp.2024.049368.

[7] T. Nurhanis, S. A. Khan, A. Khan and M. N. Akhtar, Control of base pressure at supersonic Mach number in a suddenly expanded flow, Journal of Advanced Research in Fluid Mechanics and Thermal Sciences 109(1) (2023), 210-225. https://doi.org/10.37934/arfmts.109.1.210225.

[8] A. A. Ahmad Fakhruddin, S. A. Khan, F. A. Ghasi Mahboobali, M. N. Akhtar and K. A. Pathan, Analysis of base pressure control with ribs at Mach 1.2 using CFD method, Journal of Advanced Research in Fluid Mechanics and Thermal Sciences 123(1) (2024), 108-143. https://doi.org/10.37934/arfmts.123.1.108143.

[9] A. Khan, N. M. Mazlan and M. A. Ismail, Velocity distribution and base pressure analysis of under-expanded nozzle flow at Mach 1.0, Journal of Advanced Research in Fluid Mechanics and Thermal Sciences 92(1) (2022), 177-189. https://doi.org/10.37934/arfmts.92.1.177189.

[10] F. A. Khan, A. A. Ibrahim, M. S. Rais, A. Khan and M. N. Akhtar, Performance analysis of supervised learning algorithms based on classification approach, 2019 6th IEEE International Conference on Engineering Technologies and Applied Sciences (ICETAS), IEEE, 2019, pp. 9117394. DOI: 10.1109/ICETAS48360.2019.9117394.

[11] A. Mishra, A. Khan and N. Musfirah Mazlan, Determination of shock standoff distance for wedge at supersonic flow, International Journal of Engineering Transactions A: Basics 32(7) (2019), 1049-1056. DOI: 10.5829/ije.2019.32.07a.19.

[12] Z. I. Chaudhary, A. Khan, S. A. Khan and K. A. Pathan, Base pressure control using quarter-circle rib in a suddenly expanded duct at screech prone Mach number $M = 1.8$, CFD Letters 17(8) (2025), 60-95. https://doi.org/10.37934/cfdl.17.8.6095.

[13] F. A. G. Mahaboobali, A. Khan, M. N. Akhtar, S. A. Khan and K. A. Pathan, Passive control of base flows and impact of quarter rib radius and locations at sonic Mach number, Journal of Advanced Research in Numerical Heat Transfer 30(1) (2025), 47-81. https://doi.org/10.37934/arnht.30.1.4781.

[14] Z. I. Chaudhary, A. Khan, S. A. Khan, M. N. Akhtar and K. A. Pathan, Control of suddenly expanded flow using quarter rib for area ratio 4.84 at Mach 2, Journal of Advanced Research in Experimental Fluid Mechanics and Heat Transfer 19(1) (2025), 1-29. https://doi.org/10.37934/arfmts.19.1.129.

[15] A. Khan, M. N. Akhtar, A. Aabid, M. Baig and S. A. Khan, Supersonic flow control with quarter rib in a duct: an extensive CFD study, International Journal of Thermofluids 26 (2025), 101060. https://doi.org/10.1016/j.ijft.2025.101060.

[16] S. Shetty, F. A. G. Mahaboobali, A. Khan, S. A. Khan and K. A. Pathan, Base pressure control using quarter rib at Mach 1.3: a comprehensive CFD analysis, Journal of Advanced Research in Fluid Mechanics and Thermal Sciences 127(2) (2025), 1-32. https://doi.org/10.37934/arfmts.127.2.132.

[17] S. A. I. Bellary, A. Khan, M. N. Akhtar, S. A. Khan and K. A. Pathan, Numerical simulations of base pressure and its control in a suddenly expanded duct at Mach 1.6 using quarter circular ribs, Journal of Advanced Research in Fluid Mechanics and Thermal Sciences 127(2) (2025), 203-233. https://doi.org/10.37934/arfmts.127.2.203233.

[18] S. A. I. Bellary, S. A. Dabir, J. H. Shaikh, T. Tamhane and A. Khan, Computational analysis of thrust generated by converging-diverging nozzle at different diverging angle, Journal of Advanced Research in Numerical Heat Transfer 29(1) (2025), 102-128. https://doi.org/10.37934/arnht.29.1.102128.

[19] F. N. D. M. Anuar, S. A. Khan, F. A. G. Mahaboobali, A. Khan and M. N. Akhtar, Effect of cavity geometry and location on base pressure in a suddenly expanded flow at Mach 2.0 for area ratio 3.24, Journal of Advanced Research in Applied Mechanics 117(1) (2024), 1-21. https://doi.org/10.37934/aram.117.1.121.

[20] M. Bashir, P. Rajendran, A. Khan, V. Raja and S. A. Khan, Numerical investigation of turbulence models with emphasis on turbulent intensity at low Reynolds number flows, Advances in Aircraft and Spacecraft Science 10(4) (2023), 303-315. https://doi.org/10.12989/aas.2023.10.4.303.

[21] M. A. A. Baig, S. A. Khan, F. Al-Mufadi and E. Rathakrishnan, Control of base flows with microjets, International Journal of Turbo and Jet Engines 28(1) (2011), 59-69. DOI: 10.1515/tjj.2011.009.

[22] S. Rehman and S. A. Khan, Control of base pressure with micro-jets: Part I, Aircraft Engineering and Aerospace Technology 80(2) (2008), 158-164. https://doi.org/10.1108/00022660810859373.

[23] M. Faheem, S. Afghan Khan, W. Asrar, A. Khan and R. Kumar, Experimental study on the mean flow characteristics of a supersonic multiple jet configuration, Aerospace Science and Technology 108 (2021), 106377. DOI: 10.1016/j.ast.2020.106377.

[24] M. F. M. Sajali, A. Aabid, S. A. Khan, E. Sulaeman and F. A. G. Mehaboobali, Numerical investigation of the flow field of a non-circular cylinder, CFD Letters 11(5) (2019), 37-49. https://www.akademiabaru.com/submit/index.php/cfdl/article/view/3161.

[25] S. A. Khan, M. Asadullah, G. M. Fharukh Ahmed, A. Jalaluddeen and M. A. Ali Baig, Passive control of base drag in compressible subsonic flow using multiple cavities, International Journal of Mechanical and Production Engineering Research and Development 8(4) (2018), 39-44. DOI: 10.24247/ijmperdaug20185.

[26] S. A. Khan, M. A. Fatepurwala, K. N. Pathan, P. S. Dabeer and M. A. A. Baig, CFD analysis of human-powered submarine to minimize drag, International Journal of Mechanical and Production Engineering Research and Development 8(3) (2018), 1057-1066. DOI: 10.24247/ijmperdjun2018111.

[27] S. A. Khan, Mohammed Asadullah and Jafar Sadiq, Passive control of base drag employing dimple in subsonic suddenly expanded flow, International Journal of Mechanical and Mechatronics Engineering IJMME-IJENS 18(3) (2018), 69-74.

[28] A. Aabid, M. Baig, M. A. Murtuza and S. A. Khan, Optimization of dry sliding wear behavior of aluminium-based hybrid MMC's using experimental and DOE methods, Journal of Materials Research and Technology 16 (2022), 743-763. https://doi.org/10.1016/j.jmrt.2021.12.00.

[29] E. Rathakrishnan, Effect of ribs on suddenly expanded flows, AIAA Journal 39(7) (2001), 1402-1404. https://doi.org/10.2514/2.1461.